ELSEVIER

Finite-volume transport on various cubed-sphere grids

William M. Putman [a,*], Shian-Jiann Lin [b]

[a] *NASA – GSFC Software Integration and Visualization Office – SIVO, Mail Stop 610.3, Greenbelt, MD 20771, United States*
[b] *NOAA Geophysical Fluid Dynamics Laboratory, 201 Forrestal Road, Princeton, NJ 08540-6649, United States*

Abstract

The performance of a multidimensional finite-volume transport scheme is evaluated on the cubed-sphere geometry. Advection tests with prescribed winds are used to evaluate a variety of cubed-sphere projections and grid modifications including the gnomonic and conformal mappings, as well as two numerically generated grids by an elliptic solver and spring dynamics. We explore the impact of grid non-orthogonality on advection tests over the corner singularities of the cubed-sphere grids, using some variations of the transport scheme, including the piecewise parabolic method with alternative monotonicity constraints. The advection tests revealed comparable or better accuracy to those of the original latitudinal–longitudinal grid implementation. It is found that slight deviations from orthogonality on the modified cubed-sphere (quasi-orthogonal) grids do not negatively impact the accuracy. In fact, the more uniform version of the quasi-orthogonal cubed-sphere grids provided better overall accuracy than the most orthogonal (and therefore, much less uniform) conformal grid. It is also shown that a simple non-orthogonal extension to the transport equation enables the use of the highly non-orthogonal and computationally more efficient gnomonic grid with acceptable accuracy.
Published by Elsevier Inc.

Keywords: Cubed-sphere; Finite-volume; Advection; Transport schemes; Monotonicity

1. Introduction

The finite-volume dynamical core (FV core hereafter; [1]) has been generalized for quasi-uniform cubed-sphere grids in general non-orthogonal curvilinear coordinates using the National Oceanic and Atmospheric Administration (NOAA) Geophysical Fluid Dynamics Laboratory's (GFDL) Flexible Modeling System (FMS), with the final goal of being a shared modular component within various global modeling efforts. The original FV core ([1]; L04 hereafter) on the latitudinal–longitudinal grid is already an integral component within the National Aeronautics and Space Administration (NASA) Goddard Earth Observing System (GEOS) modeling suite (e.g. [2–4]), the climate modeling efforts at NOAA/GFDL [5], and the Community Atmosphere Model at the National Center for Atmospheric Research (NCAR) [6,7]. The main objectives of

the cubed-sphere development are to avoid the numerical difficulties of the spherical poles, explore a new level of parallelism (two-dimensional X–Y domain decomposition) that is not practical within the current latitude–longitude grid construct [8], and to facilitate the development of a unified regional–global modeling system for both weather and climate applications. In addition, the cubed-sphere geometry is ideally suited for adaptive mesh refinement [9–11], which could be effectively used for tropical cyclone predictions and simulations.

The cubed-sphere grid is a projection of a cube onto the surface of a sphere represented as six adjoining grid faces which seamlessly cover the whole globe [12–15]. The cubed-sphere thus provides a quasi-uniform resolution over the whole globe, which offers several significant computational advantages over the existing latitude–longitude grid implementation. In particular, the quasi-uniform nature of the cubed-sphere grid eliminates the parallelization difficulties associated with the poles, allowing a far more efficient implementation of the horizontal 2D domain decomposition, a feature that will be required of a truly scalable ultra-high resolution global cloud-resolving model. Furthermore, the convergence of meridians near the poles on the latitude–longitude grid requires the "Flux-Form Semi-Lagrangian" (FFSL) extension for stability if a large-time-step is to be used ([16]; LR96 hereafter). Due to the extreme grid aspect ratio, the FFSL extension on the latitude–longitude grid creates a difficult load balancing issue due to a much larger halo region in the zonal direction near the poles. In the full primitive-equation implementation, a polar filter is also required to stabilize the high frequency gravity waves that are being over-resolved at high latitudes. The pole-less and quasi-uniform nature of the cubed-sphere grid eliminates all of these issues.

For atmospheric modeling purposes, the cubed-sphere is not to be regarded as the perfect solution for gridding the whole sphere, nor is any other known grid. But it is an excellent compromise when considering grid uniformity, orthogonality, and ease of applying existing high-order finite-volume transport algorithms. Regarding grid uniformity, although far superior than the latitude–longitude grid, the cubed-sphere is not as uniform as the Geodesic grid (e.g. [17–19]). But it is relatively easier to apply higher order transport algorithms due to its logically rectangular construct. It is also more natural for the implementation of a self-consistent nesting or mesh refinement capability within a regional–global modeling framework.

The original cubed-sphere grids (the gnomonic grids) are highly non-orthogonal, which impacts the accuracy of the multidimensional algorithm of LR96 used in the FV core. This is because the LR96 algorithm formally requires an orthogonal grid. To overcome the limitations on the use of the gnomonic grids, we have extended the LR96 algorithm for implementation on a general non-orthogonal curvilinear coordinate system. Alternatively, the cube can be projected onto the sphere to produce highly orthogonal conformal mappings [14]. We note, however, the conformal mapping is only orthogonal in the interior, with coordinate lines still intersecting at the 8 corners at a 120-degree angle. Therefore, some modifications to the algorithm still need to be made to counter the non-orthogonality near the corners. It would then seem advantageous to further relax the orthogonality requirement in order to allow for more uniformity, which not only enables a larger time-step, but potentially better overall accuracy.

Starting from the highly non-orthogonal gnomonic grids, one can trade some grid uniformity for improved orthogonality by various numerical grid generation techniques. One of the objectives of this paper is to study the best compromise between grid uniformity and orthogonality for the overall better accuracy and computational efficiency (size of allowable time-step) versus the extension of the LR96 algorithm on the non-orthogonal gnomonic grids.

We investigate modifications to the original gnomonic mappings of [12] by the elliptic solver grid generators (e.g. [20]) and the spring dynamics technique (e.g. [21]) to produce quasi-orthogonal mappings which preserve uniformity to a greater degree than the conformal mappings. The extent to which the improved orthogonality of the numerically modified grids improves accuracy over the original gnomonic mappings will be evaluated through standard two-dimensional advection test cases.

The organization of this paper is as follows. In Section 2, a modified form of the LR96 transport algorithm for the general non-orthogonal curvilinear coordinate on the sphere is presented. In Section 3, the gnomonic grid, the conformal grid, and the two numerically generated grids, the elliptic grid and the spring dynamics grid are inter-compared. We study, in Section 4, the sensitivity of the generalized LR96 flux-form transport scheme on the various cubed-sphere grids via a standard solid body rotation test case. The generalized LR96 algorithm is further explored on the gnomonic grid through a deformational flow experiment and a recently introduced moving vortices experiment. Summary and conclusions are provided in Section 5.

2. The multidimensional flux-form transport scheme on the general curvilinear coordinate system

The continuous differential form of the conservation law for a density-like field ρ in a general 2D curvilinear coordinate system (x, y) is

$$\frac{\partial \rho}{\partial t} + \nabla \cdot (\overrightarrow{V} \cdot \rho) = 0 \tag{1}$$

where $\overrightarrow{V}$ is the horizontal vector velocity. Following L04, the finite-volume mean of the continuous ρ field is defined as $\tilde{\rho}$

$$\tilde{\rho}(t) \equiv \frac{1}{\Delta \mathcal{A}} \int \int \rho(t; x, y) \mathrm{d}x \, \mathrm{d}y \tag{2}$$

where the surface (double) integral covers the finite-volume under consideration, and $\Delta \mathcal{A} = \int \int \mathrm{d}x \mathrm{d}y$ is the area of that finite-volume. Utilizing the divergence theorem, (1) can be integrated analytically in time (from time-step "n" to "$n + 1$") and in space (for the finite-volume):

$$\tilde{\rho}^{n+1} = \tilde{\rho}^n - \frac{1}{\Delta \mathcal{A}} \int_t^{t+\Delta t} \left[\oint \rho(t; x, y) \overrightarrow{V} \cdot \overrightarrow{n} \mathrm{d}l \right] \mathrm{d}t \tag{3}$$

where $\overrightarrow{n}$ is the normal outward vector and $\mathrm{d}l$ is the elemental length along the cell wall. The contour integral (around the finite-volume) in (3) can be approximated by decomposing the flux integral into two 1D components using 1D flux-form operators along the two independent coordinate directions. The 1D operators represent updates for one time-step to the predicted field due to the transport process from the two independent spatial directions (x, y). Defining $(\tilde{u}, \tilde{v})$ as the contra-variant and (u, v) as the covariant components of the vector wind

$$\overrightarrow{V} = \tilde{u}\overrightarrow{e_1} + \tilde{v}\overrightarrow{e_2} \tag{4}$$
$$u = \overrightarrow{V} \cdot \overrightarrow{e_1}, v = \overrightarrow{V} \cdot \overrightarrow{e_2} \tag{5}$$

and $(\widetilde{u^*}, \widetilde{v^*})$ as the corresponding time-averaged (from t to $t + \Delta t$), where $(\overrightarrow{e_1}, \overrightarrow{e_2})$ are the local unit vectors of the curvilinear coordinate system, the 1D finite-volume flux-form operator F in the x-direction can be written as

$$F(\widetilde{u^*}, \Delta t, \tilde{\rho}^n) = -\frac{\Delta t}{\Delta \mathcal{A}} \delta_x [\chi \Delta y \sin(\alpha)] \tag{6}$$

$$= -\frac{\Delta t}{\Delta \mathcal{A}} \delta_x [\widetilde{u^*} \rho^* (\widetilde{u^*}, \Delta t, \tilde{\rho}^n) \Delta y \sin(\alpha)] \tag{7}$$

where χ is the time-averaged mass flux across the cell wall

$$\chi = \frac{1}{\Delta t} \int_t^{t+\Delta t} \rho \tilde{u} \, \mathrm{d}t \equiv \widetilde{u^*} \rho^* (\widetilde{u^*}, \Delta t, \tilde{\rho}^n) \tag{8}$$

In the above derivation, ρ^* is interpreted as the time mean density value of all material passing through the cell edge from the upwind direction:

$$\rho^* (\widetilde{u^*}, \Delta t, \tilde{\rho}^n) \approx \frac{1}{\Delta t} \int_t^{t+\Delta t} \rho \, \mathrm{d}t \tag{9}$$

and the following definitions are used: Δy the local curvilinear grid length along the cell edge in the y-direction, α the "angle" between the two local unit vectors $(\overrightarrow{e_1}, \overrightarrow{e_2})$ of the curvilinear coordinate system

$$\cos(\alpha) = \overrightarrow{e_1} \cdot \overrightarrow{e_2} \tag{10}$$

and the difference operator is defined as

$$\delta_x q = q\left(x + \frac{\Delta x}{2}\right) - q\left(x - \frac{\Delta x}{2}\right) \tag{11}$$

Similarly, the 1D flux-form operator in the y-direction, G, can be written as

$$G(\widetilde{v^*}, \Delta t, \tilde{\rho}^n) = -\frac{\Delta t}{\Delta \mathcal{A}} \delta_y[Y \Delta x \sin(\alpha)] \tag{12}$$

$$= -\frac{\Delta t}{\Delta \mathcal{A}} \delta_y[\widetilde{v^*} \rho^*(\widetilde{v^*}, \Delta t, \tilde{\rho}^n) \Delta x \sin(\alpha)] \tag{13}$$

Note, in (7) and (13), the local metric factor due to grid non-orthogonality, $\sin(\alpha)$, which originated from the inner vector product in (3), reduces to unity for orthogonal grids. Following LR96, to achieve higher order accuracy, the 1D flux-form operators are applied in a directionally symmetric fashion by averaging two anti-symmetrical schemes, formally resulting in the use of four 1D flux-form operators (for two-dimensional schemes). To avoid the flow deformation induced directional splitting error, the "inner operators" are replaced by their 1D advective-form counterparts (f and g, in the x- and y-directions, respectively). Defining the following short hand notation:

$$\rho^x = \tilde{\rho}^n + \frac{1}{2} f[\widetilde{u^*}, \Delta t, \tilde{\rho}^n] \tag{14}$$

$$\rho^y = \tilde{\rho}^n + \frac{1}{2} g[\widetilde{v^*}, \Delta t, \tilde{\rho}^n] \tag{15}$$

The 2D transport algorithm can be written as

$$\tilde{\rho}^{n+1} = \tilde{\rho}^n + F[\widetilde{u^*}, \Delta t, \rho^y] + G[\widetilde{v^*}, \Delta t, \rho^x] \tag{16}$$

In principle, the inner operators can be different schemes and/or having lower order accuracy than the "outer" flux-form operators. For economical reason, one may choose a lower order scheme for the inner operator. However, it was found, on modern parallel computers with substantial inter-processor communication requirement, using the same higher order schemes (e.g. PPM vs. the second-order van Leer scheme) as "inner" operators improved the accuracy with only minimal additional computational cost. L04 derived the inner "advective-form" operators used in (14) and (15) using the same flux-form operators with an explicit divergence correction term (see Eqs. (7) and (8) in L04). To better preserve the monotonicity within the same numerical framework as in L04, the divergence correction term can be made time implicit (with no additional cost) as follows:

$$\rho^x = \frac{1}{2}\left[\tilde{\rho}^n + \frac{\tilde{\rho}^n + F}{1 + F(\rho^* = 1)}\right] \tag{17}$$

$$\rho^y = \frac{1}{2}\left[\tilde{\rho}^n + \frac{\tilde{\rho}^n + G}{1 + G(\rho^* = 1)}\right] \tag{18}$$

where

$$F(\rho^* = 1) = -\frac{\Delta t}{\Delta \mathcal{A}} \delta_x[\widetilde{u^*} \Delta y \sin(\alpha)]$$

and

$$G(\rho^* = 1) = -\frac{\Delta t}{\Delta \mathcal{A}} \delta_y[\widetilde{v^*} \Delta x \sin(\alpha)]$$

Eq. (16) together with (17) and (18) form the general 2D transport scheme that will be evaluated in subsequent sections. Practically any 1D forward-in-time finite-volume scheme can be used. LR96 and L04 argued that the PPM scheme achieves an excellent balance between accuracy and computational efficiency, and as such is our method of choice for the 1D operators. The use of the same inner and outer operator within the LR96 algorithm also avoided a potential stability issue [22]. Alternative monotonicity constraints for large-time-step has been studied in [23].

In Section 4, the performance of several schemes for determining the subgrid distributions on the cubed-sphere are investigated. These include, (i) the optimized PPM operator used within the latitude–longitude FV core, labeled as ORD = 4 (see B3 and B4 in L04), (ii) a quasi-monotonic scheme, using the base PPM with

Huynh's second constraint [24] is labeled as ORD = 5, (iii) a non-monotonic quasi-fifth-order scheme, labeled as ORD = 6 (described in full details in Appendix B), and, (iv) an extension of the ORD = 5 scheme with special treatment of edge discontinuities on the cubed-sphere grid labeled as ORD = 7 (describe in details in Appendix C).

3. The cubed-sphere grids

In our implementation, the cubed-sphere grid geometry is completely defined by the locations of the vertices (of the finite-volumes). The cell areas ($\Delta\mathcal{A}$), grid lengths in the two cartesian directions ($\Delta x, \Delta y$), and a non-orthogonal metric factor ($\sin\alpha$), where α is the angle formed at the intersection of the coordinates connecting the finite-volume vertices, are derived quantities. The cell vertices can be generated in several ways: the original gnomonic mapping based on the equidistant [12] or equiangular projections [13], the highly orthogonal conformal mapping [14], or numerical modifications to these analytical mappings by an elliptic solver (see [25] for details) or the spring dynamics generator [21]. Grid resolutions are defined in this paper as cM where M represents the number of grid cells along each of the edges of a cubed-sphere face thus the total number of cells for a given resolution is $M \times M \times 6$.

Cell areas ($\Delta\mathcal{A}$) are computed by the spherical excess formula (Eq. (19) as in [26]) given the 4-sided spherical quadrilateral for each finite-volume with internal angles ($\alpha_1, \alpha_2, \alpha_3, \alpha_4$) and the radius of the sphere R

$$\Delta\mathcal{A} = R^2[\alpha_1 + \alpha_2 + \alpha_3 + \alpha_4 - 2\pi] \tag{19}$$

The cell edges for all grids are prescribed to be great circle arcs and thus this formula for the cell area is exact and only degenerates on a perfectly orthogonal grid where $[\alpha_1 + \alpha_2 + \alpha_3 + \alpha_4 - 2\pi] = 0$. The grid lengths ($\Delta x, \Delta y$) are thus computed by great circle distances. Given the latitude–longitude coordinate of two points on the sphere (λ_1, θ_1) and (λ_2, θ_2) the great circle distance δh can be computed as

$$\delta h = R\cos^{-1}[\cos\theta_1\cos\theta_2\cos(\lambda_1 - \lambda_2) + \sin\theta_1\sin\theta_2] \tag{20}$$

An alternative form, which is less sensitive to rounding errors for small angles can be used based on the angle τ between two vectors $\vec{V}_1, \vec{V}_2$ connecting from the center of the sphere to the two points

$$\vec{V}_i = R(\cos\theta_i\cos\lambda_i, \cos\theta_i\sin\lambda_i, \sin\theta_i) \tag{21}$$

$$\tau = \cos^{-1}\left(\frac{\vec{V}_1 \bullet \vec{V}_2}{R^2}\right) \tag{22}$$

$$\delta h = \sin\left(\frac{\tau}{2}\right) = 2\arcsin\left(\sqrt{\sin^2\left(\frac{\theta_2 - \theta_1}{2}\right) + \cos\theta_1\cos\theta_2\sin^2\left(\frac{\lambda_2 - \lambda_1}{2}\right)}\right) \tag{23}$$

3.1. Gnomonic projection

The gnomonic mapping of the cubed-sphere is obtained by inscribing a cube within a sphere and expanding to the surface of the sphere [14]. A local cartesian coordinate system is determined for each of the six faces of the cube, and a transformation is applied to connect each point on the cube to the spherical surface. There are two choices for the local coordinates on the faces of the cube. The mapping between local coordinates $(x, y)_f$, ranging from $[-a, +a]$ for cube faces $f \in 1, 6$ where $a = \frac{\sqrt{3}}{3}R$ and spherical coordinates (X, Y, Z) for the local face centered in the $-Y$ direction with an equidistant gnomonic mapping on a sphere of radius R takes the form

$$(X, Y, Z) = \frac{R}{r}(x, -a, y)$$
$$r = \sqrt{a^2 + x^2 + y^2}.$$

Alternatively, a gnomonic mapping can be defined based on an equiangular projection where local coordinates are defined as

$$x = a \tan x_0$$
$$y = a \tan y_0$$

where the coordinates (x_0, y_0) range from $(-\pi/4, +\pi/4)$. The equiangular projection at 2-degree resolution is displayed in Fig. 1c. The equiangular projection leads to a more uniform distribution of grid cells on the sphere than the equidistant projection and an ideal scaling of the minimum grid length with increasing resolution (Fig. 2). Either choice of gnomonic projection produces a cubed-sphere mapping which is highly non-orthogonal and non-conformal. A conformal mapping is one in which the angles are preserved between intersecting smooth curves [14]. The gnomonic mapping produces a sharp angular discontinuity across the edges of the cube faces. The conformal mapping maintains a smooth transition across these edges and produces the optimal orthogonality for the cubed-sphere grid.
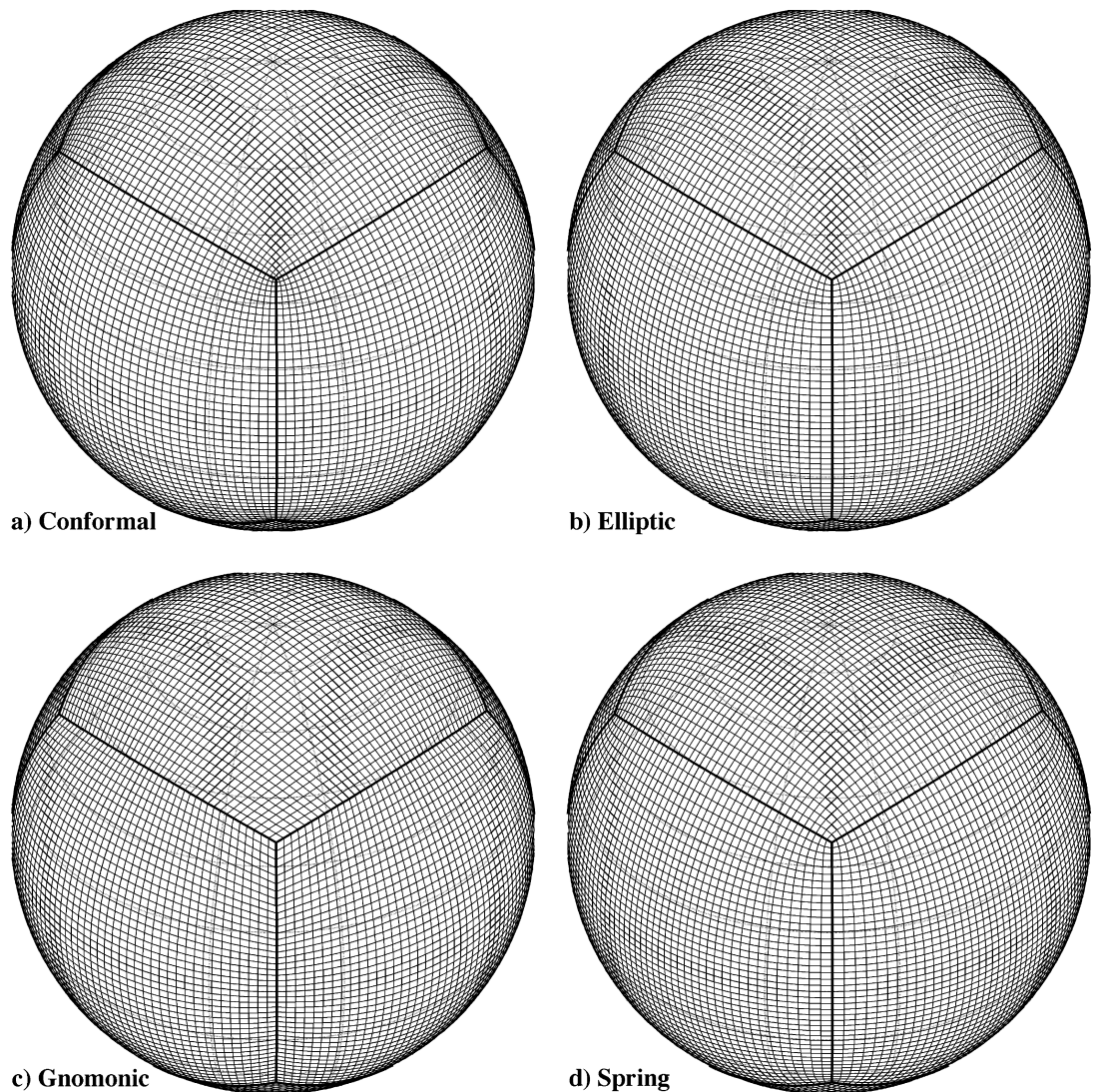

Fig. 1. The cubed-sphere grids at 2° (c44) resolution displaying cells on the sphere, the image focuses on the distribution of grid cells near one corner of the grid; (a) conformal mapping, (b) the gnomonic grid modified by elliptic solver, (c) equiangular gnomonic mapping and (d) the gnomonic grid modified by spring dynamics.
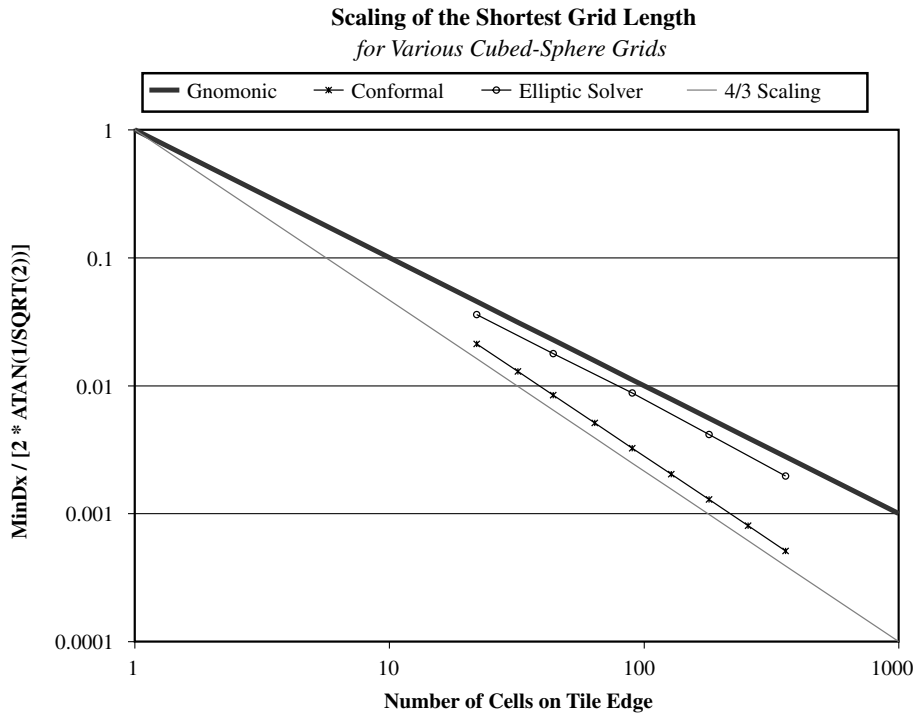
Scaling of the Shortest Grid Length

for Various Cubed-Sphere Grids

Fig. 2. Scaling of the minimum grid length with increasing resolution for the gnomonic, conformal and elliptic cubed-sphere grid mappings.

3.2. Conformal projection

A conformal projection preserves the angles between intersecting curves on adjoining faces of the cubed-sphere and is differentiable to any order at all points except the eight singularities. The conformal mapping is obtained as described in [14] via a reversible sequence of transformations between a plane and the sphere using a stereographic projection and a Taylor series to complete the transformation from the intermediate stereographic plane. The conformal projection (Fig. 1a) produces a grid with exceptional orthogonality traits and a near uniform aspect ratio $\left(\frac{\Delta x}{\Delta y} = 1\right)$ throughout the sphere. The corner singularities remain non-orthogonal with angular deviation from 90° fixed at 30°, the vertices surrounding the corner also remain slightly non-orthogonal with the first grid point off the corner maintaining a deviation from orthogonality near 8.5° regardless of grid resolution. The strict orthogonality constraints on the conformal mapping lead to a convergence of grid cells near the eight singularities of the grid. While this convergence is far less severe than that of the latitude–longitude grid at the spherical poles, the scaling of minimum grid length with resolution is far from ideal. Stretching factors can be used to rescale the conformal mapping [26], or elliptic solvers or spring dynamics techniques may be applied to reduce this convergence near the corners while maintaining strong orthogonality constraints. Stretching does not compromise the conformal attributes of the grid, nor the superior orthogonality traits of the conformal mapping. However, stretching leads to severe aspect ratio distortion along the edges of each face as resolution increases, distortion so severe that it prevents effective stretching of the conformal mapping for producing efficient high resolution grids.

3.3. Elliptic solvers

Elliptic grid generation is the iterative relaxation of a first-guess grid (via successive over-relaxation) to satisfy a quasi-linear elliptic system of partial differential equations (PDEs) while imposing smoothness and orthogonality constraints [20]. In the case of the cubed-sphere, the initial grid is the original equiangular

gnomonic projection of the cubed-sphere. Each face of the physical grid in spherical coordinates is mapped to a two-dimensional *u-v* parametric space (scaled from 0 to 1 in the *X–Y* direction). The elliptic solver solves the system of PDEs in parametric space while imposing the desired physical constraints; orthogonality and uniform grid spacing are the most important constraints for this application. The symmetry of the cubed-sphere can be exploited to reduce the number of points that actually need to be run through the elliptic solver; calculations can be performed on $\frac{1}{8}$-th of a single face and the solution can be mapped symmetrically to the rest of the cubed-sphere.

There are two options for imposing orthogonality constraints: the Neumann constraint that allows the grid points to slide along the boundary of each face, and the Dirichlet constraint that holds the edge points fixed while adjusting the interior points and maintaining a quasi-uniform grid cell spacing. The Neumann approach computes a shift for each grid point along the boundary of the grid by forcing the dot product of $u \cdot v$ to be equal to zero; this approach will produce a convergence of grid cells near the corners. To limit this convergence, a weighting function can be applied to the first *n* grid points off the corner along each boundary of the grid (Eq. (24)). The weight, *rwgt*, and *n* become tunable parameters to enforce a significant amount of dependence on the orthogonality constraint while limiting the minimum grid length at the corners by the desired amount (this implementation limits convergence to grid lengths to ∼60% of the representative resolution or greater.) The *rwgt* ranges from 0.0 to 1.0, with typical values between 0.7 and 1.0

$$wt = \text{MIN}\left(1.0, \ \text{LOG}\left(\frac{i}{n}\right)^{rwgt\left(1.0-\frac{i}{n}\right)}\right) \tag{24}$$

Orthogonality may also be imposed through the use of orthogonal control functions, the Dirichlet approach. These functions are evaluated at the boundary to impose orthogonality, while maintaining the original grid spacing along the boundaries. Transfinite interpolation is applied to interpolate the control functions from the boundary to the interior of the grid. In addition, a blending function can be applied to force the interior points to remain close to the original grid spacing. The blended control function can be used to impose orthogonality and smoothing constraints within the elliptic solver.

A combination of these techniques allows the boundary points to slide a little to force orthogonality with the Neumann constraint while blending uniformity and orthogonality functions throughout the domain with the Dirichlet constraint. This leads to the quasi-orthogonal elliptic cubed-sphere grid with constraints on orthogonality while maintaining a reasonable minimum to maximum grid cell length ratio. The elliptic solver is initially run to convergence with the Neumann constraint and a given weight (*rwgt*) which varies with resolution to limit convergence to ∼0.6 of the representative resolution. Typical weights for each resolution are determined via experimentation to be (1.00, 0.925, 0.875, 0.800, and 0.775 for the resolutions 4° (c22), 2° (c44), 1° (c90), 0.5° (c180), and 0.25° (c360) respectively with a value of $n = 0.25 * npts$). The resulting grid is then run to convergence with a smoothed Dirichlet constraint to enforce orthogonality/uniformity throughout the remainder of the grid while keeping the edge lengths fixed. The result is a set of cubed-sphere grids (a c44 example is presented in Fig. 1b) with smoothly varying coordinate lines at cell edges and mean orthogonality similar to the conformal grid, while restricting quasi-orthogonality to the immediate vicinity of the singularities. As resolution increases, the aspect ratio grows along the edges of each face due to a stretching of grid lines away from the face edges, however the maximum grid length remains much less ∼2 times the representative resolution.

3.4. Spring dynamics

The spring dynamics modifications [21] to the cubed-sphere are formulated on a 3D cartesian coordinate system. Two types of springs are used; the compression type and the torsion type (our modification to the spring dynamics technique). The compression springs mostly made the grid more spatially uniform whereas the torsion springs are for enforcing orthogonality by nudging the vertices in the direction that reduces the local deviation from orthogonality. With the spring dynamics generator, one can tune the strength of the springs to obtain grids that are (i) more orthogonal, (ii) more uniform, (iii) have a larger minimum grid length (to allow larger time-step), or (iv) a compromise of the above. The spring tensions can be tuned to produce

Table 1
Grid length (in kilometers) characteristics for the conformal, elliptic and spring cubed-sphere grids for increasing resolution from 4° (c44) to 0.25° (c360)

Resolution	Conformal			Elliptic			Spring		
	Min	Max	Min/Mean	Min	Max	Min/Mean	Min	Max	Min/Mean
c22	166	471	0.43	281	522	0.67	262	567	0.63
c44	66	235	0.33	140	288	0.67	134	289	0.64
c90	25	115	0.26	69	152	0.67	59	149	0.57
c180	10	58	0.20	33	80	0.63	29	73	0.57
c360	4	29	0.16	15	44	0.60	–	–	–

quasi-orthogonal mappings in a similar way as the Neumann and Dirichlet constraints in the elliptic solver. Grids generated by the spring dynamics (a c44 example is presented in Fig. 1d) tend to have smoother solutions and fewer numerical artifacts than the elliptic solver grids. However, both techniques suffer from slow convergence rates (for the generation), especially at fine resolutions c360 and finer. However for typical global climate/weather applications this is a one-time procedure for a given resolution. Numerically modified grids (such as the spring and elliptic grids) are not ideal for adaptive mesh refinement applications since refinements to the grid would require further iterations and is thus not suitable for dynamic refinement. The gnomonic grids, particularly at high resolutions, would seem to be ideal from the mesh refinement perspective.

3.5. Grid characteristics summary

We examine the characteristics of the gnomonic, conformal, elliptic and spring grids with an emphasis on minimum grid length, orthogonality, and uniformity. Sample grids of the conformal mapping, modified elliptic, and spring-dynamics grids are presented in Fig. 1. The minimum grid length for the conformal grid reduces dramatically with increasing resolution, making the conformal mapping an inefficient choice for high resolution global modeling. The grids modified by the elliptic solver or spring dynamics have been tuned to overcome this convergence problem (Table 1) by limiting the convergence to between ∼0.5 and ∼0.6 ratio of shortest to mean grid lengths. Closer examination of the convergence of the minimum grid length with increasing resolution (Fig. 2) reveals that the elliptic grids are converging at a much slower rate than the conformal mapping and on a similar slope to the ideal gnomonic mapping (this is also the case for the spring grids, not shown).

The numerically modified grids have also been tuned to prevent severe distortion in aspect ratio along face edges (Table 3). The distribution of resolution across the sphere (uniformity, as represented by the cell area) remains unchanged for the conformal and elliptic grids, while slight variations exists in the spring grids. Slight non-orthogonality is present in the immediate vicinity of the corners, even with the conformal mapping. The non-orthogonality converges with resolution for the conformal and elliptic grids as evidenced by the maximum and mean angle deviation from orthogonality (Table 2). The spring dynamics are producing smooth grids with efficient uniformity and minimum/maximum grid length characteristics, but are not producing the most efficient grids in terms of orthogonality. With further tuning it is expected that the spring dynamics modified grids can produce orthogonality convergence characteristics similar to the elliptic grids.

Table 2
As in Table 1 but for angle deviation from orthogonality

Resolution	Conformal		Elliptic		Spring	
	Max	Mean	Max	Mean	Max	Mean
c22	8.52	1.13	13.87	1.89	9.36	0.99
c44	8.53	0.65	12.79	1.13	11.97	0.84
c90	8.53	0.34	11.97	0.69	10.93	0.51
c180	8.53	0.17	11.64	0.43	14.20	0.52
c360	8.53	0.09	11.43	0.24	–	–

Table 3
As in Table 1 but for aspect ratio (Δx:Δy)

Resolution	Conformal		Elliptic		Spring	
	Max	Mean	Max	Mean	Max	Mean
c22	1.09	1.07	1.33	1.10	1.50	1.20
c44	1.09	1.04	1.50	1.14	1.54	1.20
c90	1.09	1.02	1.77	1.16	1.67	1.24
c180	1.09	1.01	1.97	1.17	1.50	1.14
c360	1.09	1.00	2.25	1.17	–	–

4. Numerical experiments

The coordinates at the 12 interfaces between any two adjoining faces of the cubed-sphere are discontinuous, except the conformal grid where all edges are continuously differentiable excluding the eight corners. We evaluated four different variations (ORD = 4–7) to subgrid piecewise parabolic reconstruction. Except the ORD = 7 scheme, all schemes treated the interfaces as if they were continuous. The ORD = 4 scheme is the optimized monotonic PPM described in L04, which behaves nearly the same as the original PPM except that total operation count has been reduced. The ORD = 5 scheme is the same as ORD = 4 but with the monotonicity constraint replaced by Hunyh's second constraint. The ORD = 6 scheme uses instead a fifth-order interpolation for obtaining the edge values that are left unlimited (Appendix B). The ORD = 7 scheme (Appendix C) is a further modification to ORD = 5 scheme with the face edges treated more accurately as discontinuities. For all schemes tested on all grids, mass is conserved to machine precision. Three types of the prescribed advective winds are used: solid body rotation, deformational flow, and a combination of these producing moving vortices, as described below.

4.1. Solid body rotation of a cosine bell

The 2D advection test case of [27] (a solid body rotation of a cosine bell) is used to evaluate the transport algorithm derived in Section 2 on the gnomonic, conformal, elliptic and spring cubed-sphere grids. The following parameters for the radius of the earth (R), the rotation rate (Ω) and the acceleration due to gravity (g)

$$R = 6.37122 \times 10^6 \text{ m}, \quad \Omega = 7.292 \times 10^{-5} \text{ s}^{-1}, \quad g = 9.80616 \text{ ms}^{-2}$$

are used for this test. The initial height field is a cosine hill given by

$$h(\lambda, \theta) = \begin{cases} \left(\frac{h_0}{2}\right)\left(1 + \cos\left(\frac{\pi r}{R_0}\right)\right), & \text{if } r < R_0 \\ 0, & \text{if } r \geqslant R_0 \end{cases} \tag{25}$$

where $h_0 = 1000$ m, $R_0 = R/3$ and r is the great circle distance between (λ, θ) and the center, initially given at $(\lambda_c, \theta_c) = \left(\frac{3\pi}{2}, 0\right)$.

The wind components normal to the cell walls can be explicitly defined on the C-Grid by taking the derivative of the prescribed streamfunction, Eq. (26)

$$\psi = -Ru_0(\sin\theta\cos\beta - \cos\lambda\cos\theta\sin\beta), \tag{26}$$

$$u = -\frac{\partial\psi}{\partial y}, \tag{27}$$

$$v = \frac{\partial\psi}{\partial x}, \tag{28}$$

or computing directly in component form on a latitude–longitude orientation ($u_{\lambda\theta}, v_{\lambda\theta}$) using the analytic form, Eq. (29) and (30), as in [27] and re-orienting to the cubed-sphere geometry (u, v) as in Appendix A

$$u_{\lambda\theta} = u_0(\cos\theta\cos\beta + \sin\theta\cos\lambda\sin\beta) \tag{29}$$

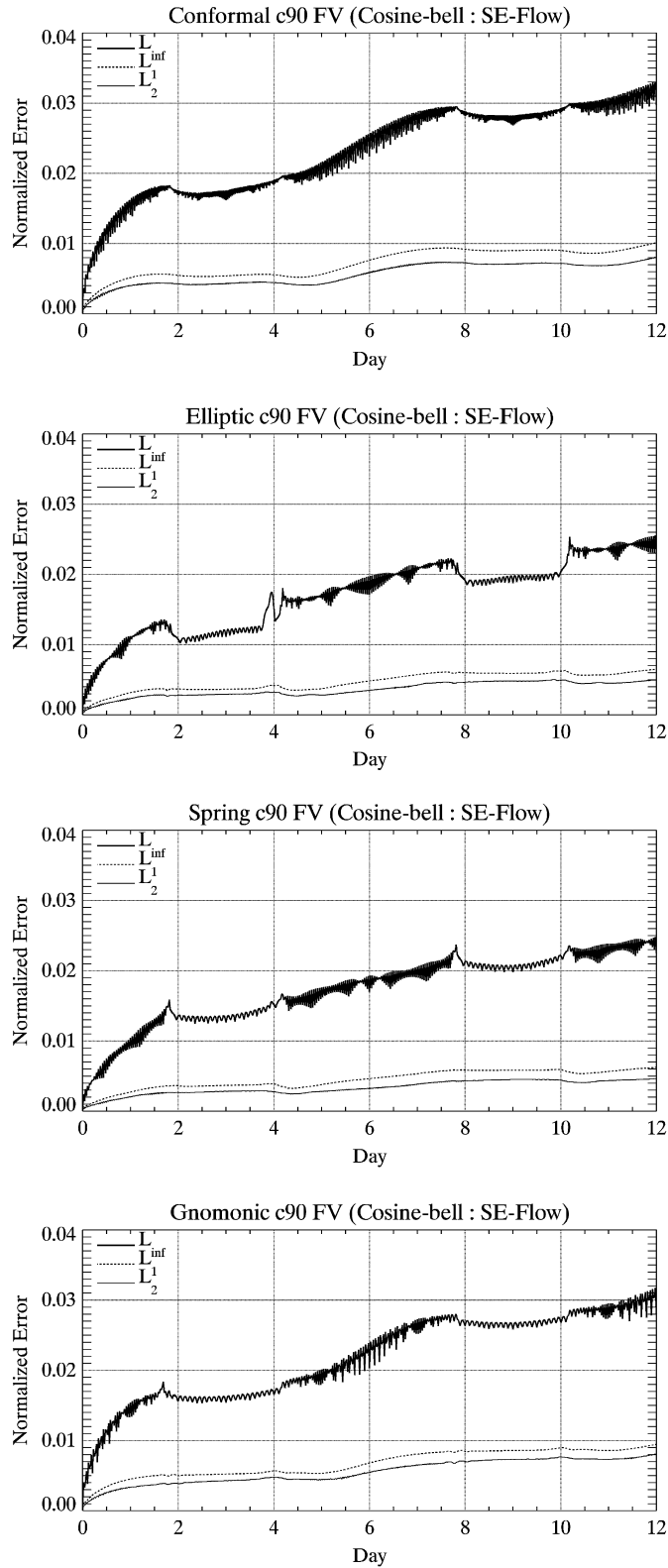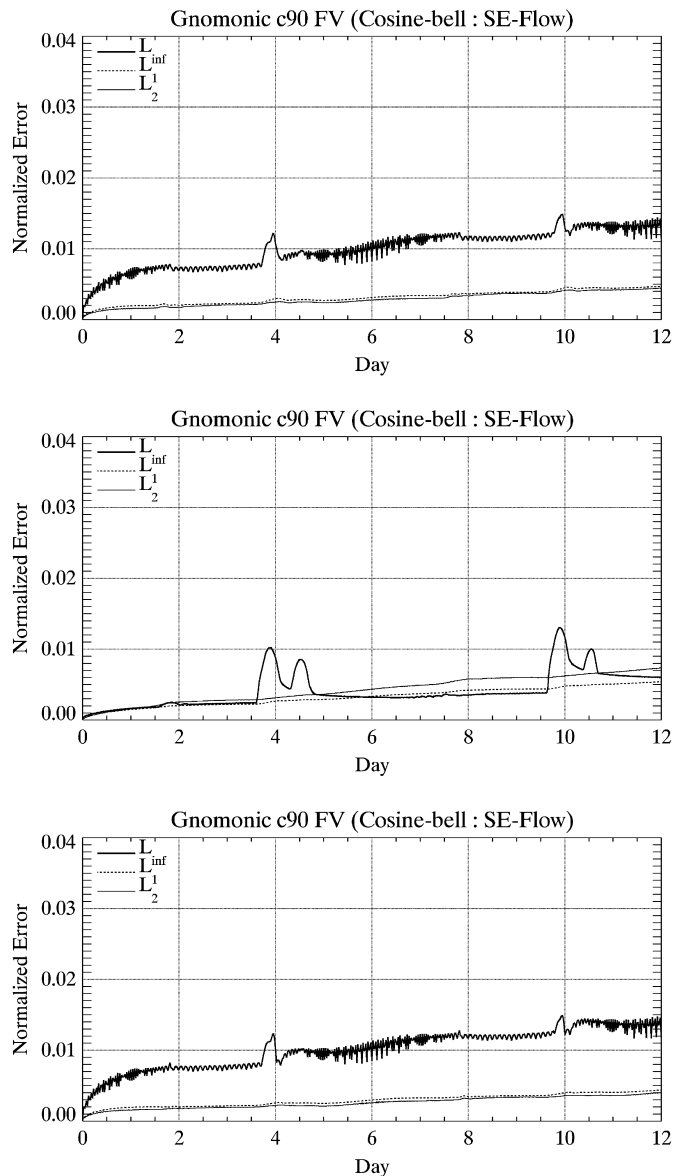$$v_{\lambda\theta} = -u_0\sin\lambda\sin\beta \tag{30}$$

Fig. 3. Time traces of normalized l_1, l_2 and l_∞ errors for the cosine bell advection test with southeastward flow oriented over the corners of the cubed-sphere with the ORD = 4 advection scheme on multiple cubed-sphere grids at c90 (1°) resolution.

where β is the angle between the axis of solid body rotation and the polar axis of the spherical coordinate system, and $u_0 = (2\pi R)/(12 \text{ days})$. The corresponding contra-variant components are simply

$$\tilde{u} = \frac{u}{\sin(\alpha)}, \quad \tilde{v} = \frac{v}{\sin(\alpha)} \tag{31}$$

where α is the "local" angle of the coordinate system, (as defined by Eq. (10)). Solid body rotation experiments reveal the choice of methods for defining the initial winds to be insignificant and all experiments herein use winds defined in component form and re-oriented to the cubed-sphere geometry.

Fig. 4. Time traces of normalized l_1, l_2 and l_∞ errors for the cosine bell advection test with southeastward flow oriented over the corners of the cubed-sphere for the gnomonic mapping using advection schemes top) ORD = 5, middle) ORD = 6 and bottom) ORD = 7.
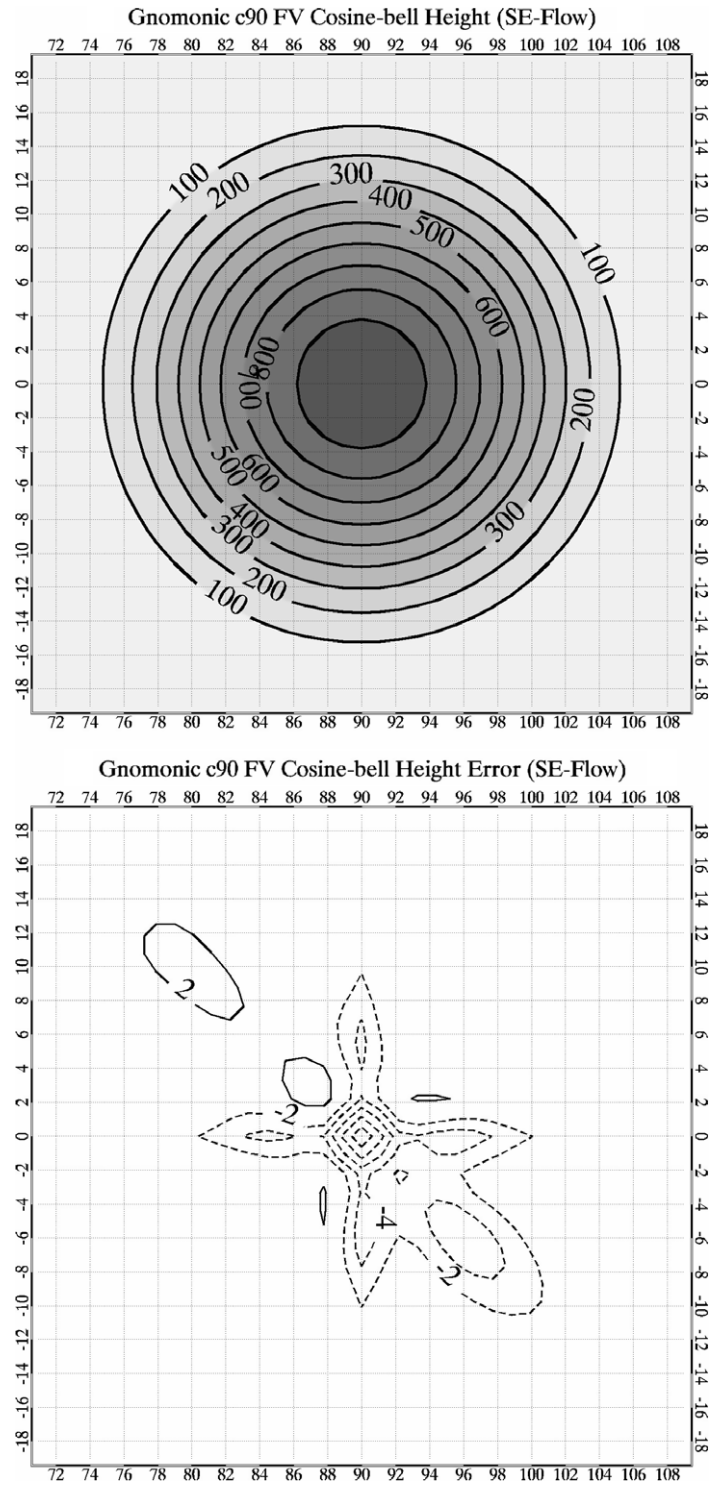
Fig. 5. The results from the solid body rotation of a cosine bell after one revolution (12-days) with southeastward oriented flow over the corners of the gnomonic cubed-sphere grid at c90 resolution. Top) The analytic solution is display as solid black contours at a 100 m contour interval, the results of the 12-day simulation on the gnomonic grid with ORD = 7 are shaded. Bottom) The difference between the analytic solution and the 12-day simulation on the gnomonic grid with ORD = 7, contours are displayed every 2-m (solid contours are positive, dashed are negative.)

4.2. Deformational flow

A deformational flow test in spherical geometry (a detailed description of this test is available in the following references [28–30]) is used to further evaluate the generalized FV advection scheme on the gnomonic cubed-sphere. This test is an idealized cyclogenesis problem where two steady vortices are generated, centered over two corners of the cubed-sphere geometry in a rotated spherical coordinate system where the north pole is located at $(\lambda_0, \theta_0) = (\pi - 0.8, \pi/4.8)$.

4.3. Moving vortices

The moving vortices experiment is an extension of the deformational flow test combined with a solid body rotation to form two moving vortices over the surface of the sphere (details can be found in [31].) The horizontal velocity components become time-dependent and are updated at every time-step based on the location of the vortex centers along a pre-determined great-circle trajectory. In our case, the trajectory is chosen such that the vortex centers pass over four corners and along two edges of the cubed-sphere.

4.4. Results

We first evaluated the conformal, gnomonic, elliptic and spring grids at varying resolutions increasing from c12 (8°) to c192 (0.5°) for the solid body rotation test case. While varying grid resolutions and flow orientations were studied, results are presented for each scheme with southeasterly flow $\left(\beta = \frac{\pi}{4}\right)$ oriented over four corners and 2 face edges of the cubed-sphere at the c90 (1°) resolution. To maintain stability, the conformal grid is tested with a time-step of 900 s, while all other grid types use a time-step of 1800 s. The standard l_1, l_2, and l_∞ normalized errors as in [27] are evaluated at each time-step throughout one full revolution of the cosine bell.
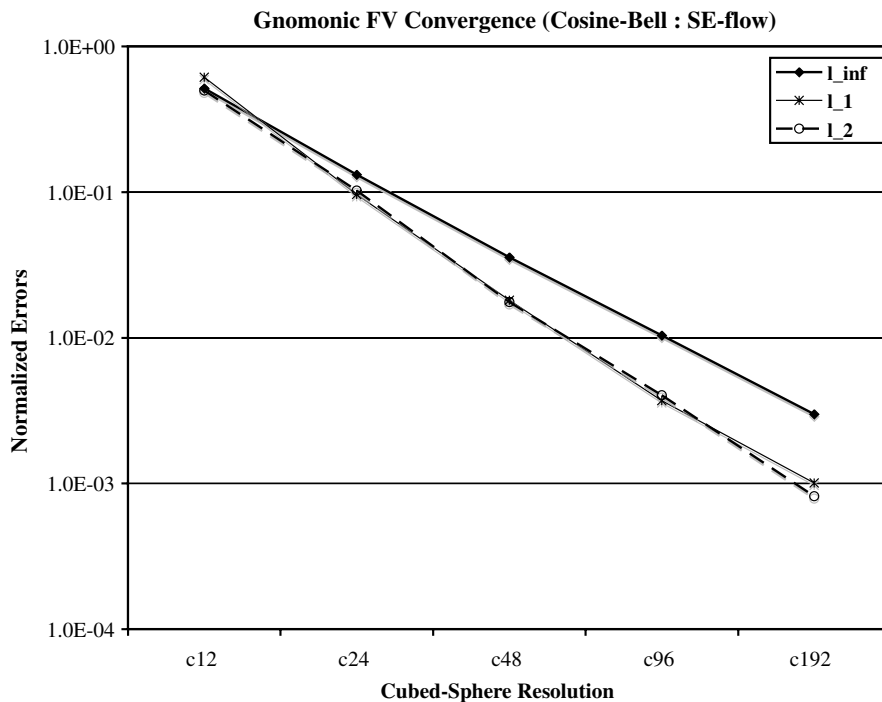

Fig. 6. Convergence of normalized l_1, l_2 and l_∞ errors for the solid body rotation of a cosine bell test after one revolution (12-days) with southeastward oriented flow over the corners of the gnomonic cubed-sphere grid with the ORD = 7 advection scheme at resolutions of c12, c24, c48, c96, and c192.

For the ORD = 4 scheme, time-traces of the normalized errors are presented in Fig. 3. The elliptic and spring grids produce the smallest errors as they have been tuned to obtain a compromise between orthogonality, grid uniformity and smoothness. Even though the 12 face edges were naively treated as continuous, there is no evidence of spurious spikes in the standard errors as the cosine bell passes smoothly over the corners on the grid and along the face edges exhibiting no signs of discontinuity. While the elliptic and spring grids do produce the smallest errors, the gnomonic grid is slightly outperforming the conformal grid, and it is evident that the gnomonic grid provides sufficiently accurate results. Since it allows the largest possible time-step, all further tests presented in this paper will use the gnomonic grid projection.

Fig. 4 shows the time-traces of the normalized errors for the same cosine bell solid body rotation test on the gnomonic grid for the other three finite-volume subgrid distribution schemes (ORD = 5, ORD = 6, and ORD = 7). The non-monotonic ORD = 6 scheme produces significantly smaller l_∞ errors, while the global errors are increased, relative to ORD = 5 and ORD = 7 schemes. The ORD = 5 and ORD = 7 schemes apply Hunyh's second constraint thus limiting the undershoots to near machine precision while the ORD = 6 is non-monotonic leading to much larger negative values (-10^{-3}). With the ORD = 7 scheme, all errors are slightly

Table 4
Normalized errors for the solid body rotation of a cosine bell on a c32 gnomonic cubed-sphere grid with southeasterly oriented flow for the ORD = 4, ORD = 5, ORD = 6 and ORD = 7 advection schemes

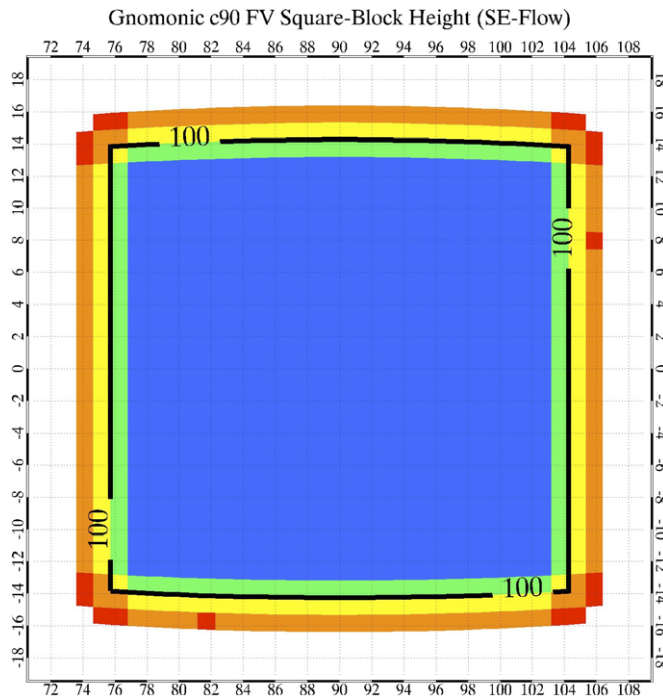| Grid	Scheme	DT	Min	l_1	l_2	l_∞
Gnomonic	FV ORD = 4	5400	3.369E−67	0.072	0.079	0.140
Gnomonic	FV ORD = 5	5400	−7.813E−26	0.048	0.045	0.072
Gnomonic	FV ORD = 6	5400	−1.271E−02	0.089	0.054	0.048
Gnomonic	FV ORD = 7	5400	1.308E−70	0.047	0.045	0.074

Fig. 7. The initial square block (heavy contour) and the final height field (shaded, values >15 – red, >35 – orange, >55 – yellow, >75 – green, >95 – blue) after one revolution (12-days) with southeastward oriented flow over the corners of the gnomonic cubed-sphere grid at c90 resolution with the ORD = 7 advection scheme. (For interpretation of the references to colour in this figure legend, the reader is referred to the web version of this article.)

reduced with the special edge treatment at the 12 discontinuous interfaces of the cubed-sphere. Due to this and its monotonicity characteristics results presented from this point use exclusively the ORD = 7 scheme.

The spatial distribution of the height field after one 12-day revolution and the difference from the exact solution is presented in Fig. 5. There is no clear distinction between the exact solution and the simulated height field (top panel). Bottom panel reveals the largest error (about 1% of the exact) to be centered at the peak of the cosine bell structure, which is due to the expected clipping effect from the monotonicity constraint.

The convergence of the ORD = 7 scheme is displayed for the solid body rotation test case (Fig. 6). These results compare directly to Fig. 8b of [30] for the convergence of the discontinuous Galerkin (DG) scheme on the cubed-sphere. Error levels with the FV scheme on the gnomonic cubed-sphere grid are consistent with the higher order DG scheme. The FV convergence rates for the solid body rotation are 1.97, 2.54 and 2.68 for the l_∞, l_2, and l_1 errors respectively. Due to the more uniform cubed-sphere geometry and the improved inner
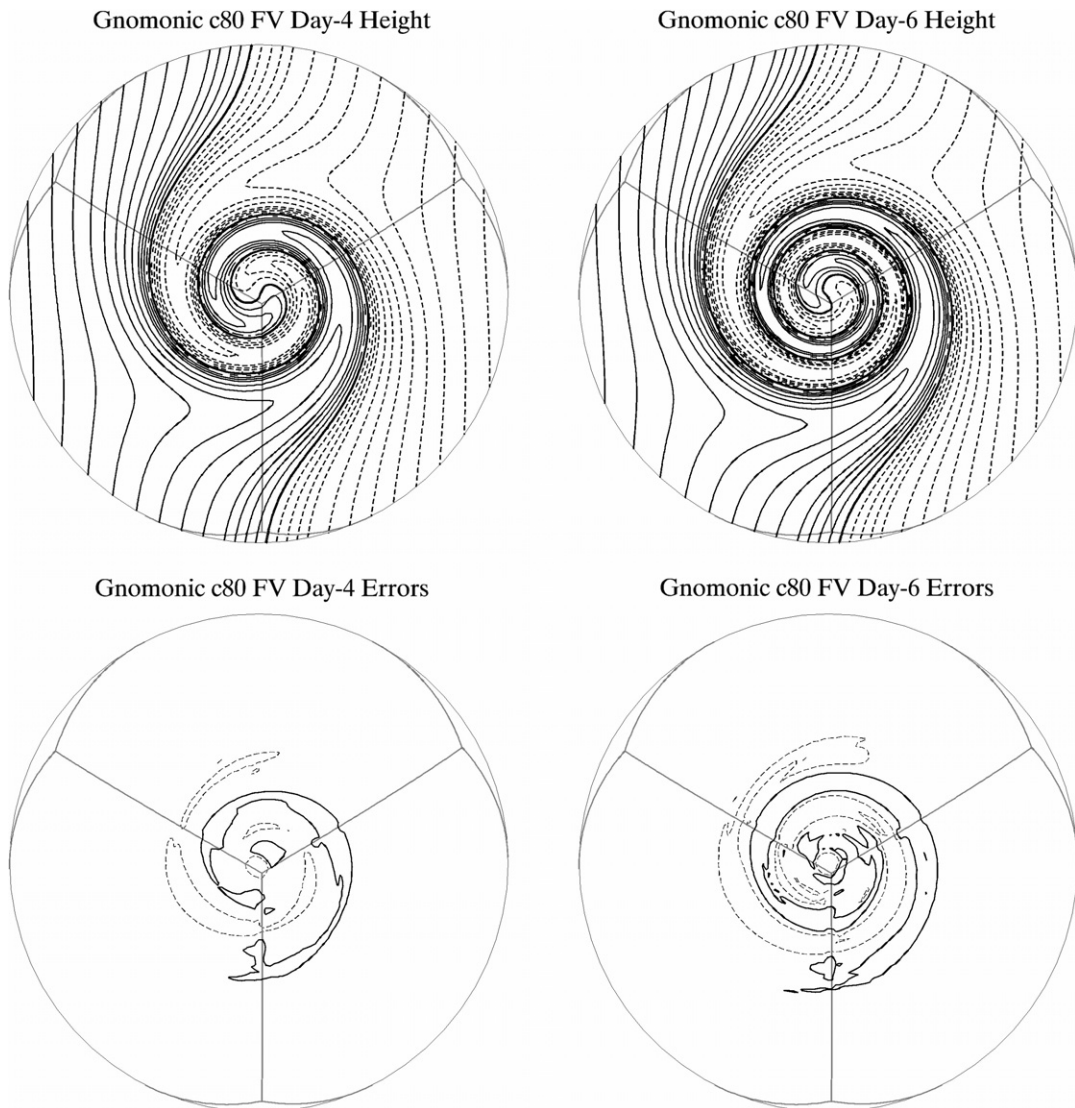

Fig. 8. The results from the static deformational flow with vortices centered on the corners of the gnomonic cubed-sphere grid at c80 resolution. The height field and difference from the analytic solution are presented at days 4 and 6 of the simulation. The height field plots contours from 0.5 to 1.5 with solid contours for values >1 and a heavy solid contour for the contour = 1. Error plots display the ±0.001 contours with negative values dashed.

operators given by (17) and (18), these results are more accurate than the original LR96 algorithms on the latitude–longitude grid at similar resolutions.

The results from each subgrid distribution scheme on the gnomonic grid are summarized in Table 4 at the c32 resolution, comparable to the 128×64 resolution used for the latitude–longitude grid in LR96 and the results presented in Table 3 of [32] summarizing the results of various schemes (including the Semi-Lagrangian inherently conserving and efficient (SLICE), the cell-integrated Semi-Lagrangian (CISL), conservative cascade scheme (CCS) and a 2D forward-in-time upwind-biased flux-form scheme extended to the 'reduced spherical grid' (RG2.8)) for rotation over the spherical poles. The FV gnomonic cubed-sphere results for the l_1 and l_2 errors for the ORD = 5 and ORD = 7 schemes over the corner singularities produce the smallest errors, better than any scheme presented with flow over the spherical poles, while the l_∞ errors are comparable to the SLICE, CISL, and FFSL-4/FFSL-5 schemes.

A similar test case to that of [27] is designed to demonstrate the shape-preserving nature of the monotonicity constraints within the finite-volume transport schemes. A square block with $h_0 = 100$ m is advected over the corners with the ORD = 7 scheme on the gnomonic c90 grid with a time-step of 1800 s. Fig. 7 displays the final height field after one full rotation over the corners. Overshoots and undershoots are clearly controlled by the monotonic constraint, as there are no significant negative values. The edges of the block are smoothed, however the peak value of the block is maintained and the general structure is preserved. Normalized errors for this case are $l_\infty = 6.39\mathrm{e}{-1}$, $l_1 = 1.32\mathrm{e}{-1}$, and $l_2 = 1.99\mathrm{e}{-1}$.

Results from the deformational flow test on the c80 gnomonic cubed-sphere grid with the FV ORD = 7 scheme and a 3600 s time-step are presented in Fig. 8. The top panels show the simulated vortices at days 4 and 6, and the bottom panels display the difference from the exact solution. The vortices (simulated at diametrically opposite vertices on the cubed-sphere as in [30]) are well resolved and differences from the numerical solution by day 6 are on the order of $\pm 1\mathrm{e}{-3}$. Further, there are no noticeable impacts of discontinuities along the face edges, the errors reveal only a slight diffusion in the simulation as compared with the exact solution.
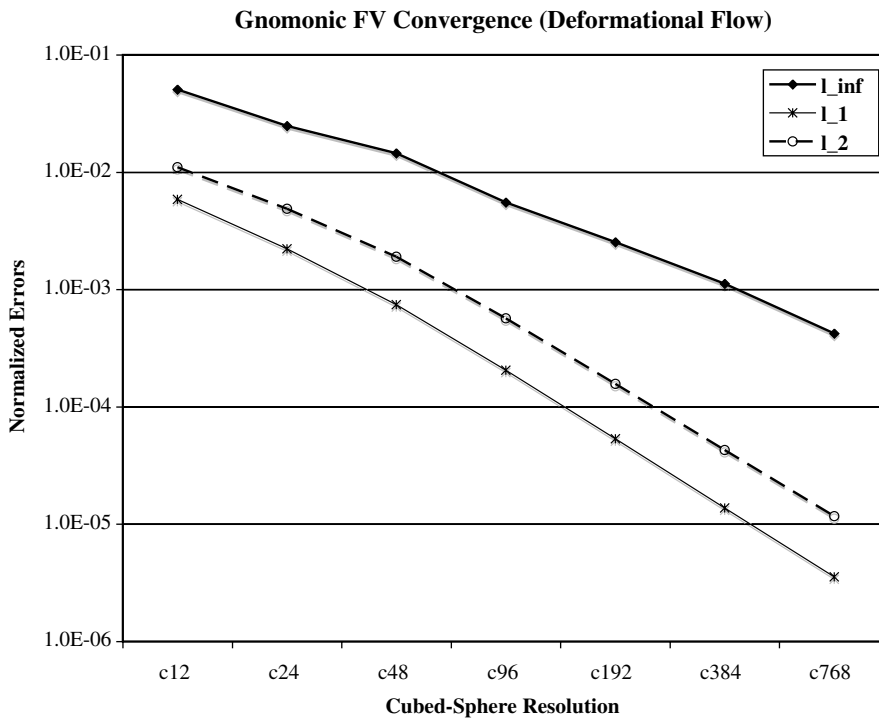

Fig. 9. Convergence of normalized l_1, l_2 and l_∞ errors for the static deformational flow with vortices centered on the corners of the gnomonic cubed-sphere grid with the ORD = 7 advection scheme at resolutions ranging from c12 to c768.

Gnomonic c80 FV Day-6 Moving Vortices Height Field

Gnomonic c80 FV Day-9 Moving Vortices Height Field

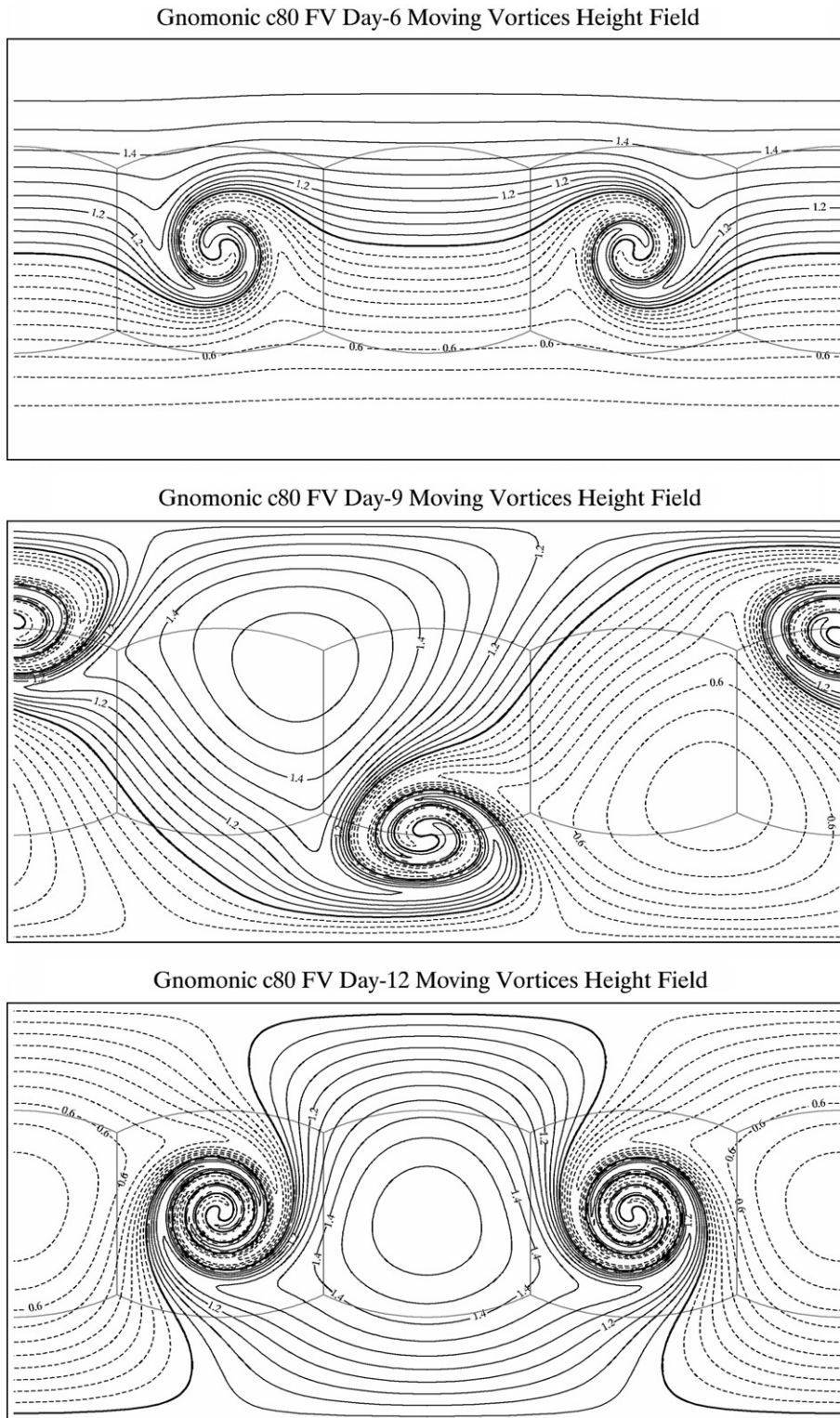Gnomonic c80 FV Day-12 Moving Vortices Height Field

Fig. 10. The results from the moving vortices test case with flow oriented over the corners of the gnomonic cubed-sphere grid at c80 resolution. The height field is presented at days 6, 9 and 12 of the simulation. Contours range from 0.5 to 1.5 with solid contours for values >1 and a heavy solid contour for the contour = 1.

The convergence of the standard l_1, l_2, and l_∞ normalized errors at day-6 are presented in Fig. 9 and they compare favorably with results presented in [30] for the DG scheme on the cubed-sphere.

Results from the recently developed moving vortices test case of [31] are presented in Fig. 10 and the difference from the exact solution is presented in Fig. 11. The flow of the solid body rotation aspect of this case is oriented southeasterly advecting the simulated vortices over four corners and two face edges of the c80 gnomonic cubed-sphere. The FV ORD = 7 scheme is used for this simulation with an 1800 s time-step. The vortices are again well resolved throughout the 12-day simulation, errors grow (isolated in the vicinity of the generated vortices) on the order of three percent of the value of the exact height field. The time-traces of the normalized l_1, l_2, and l_∞ errors are presented in Fig. 12 and can be compared directly to results presented in Fig. 7 of [31] for the FV scheme on the latitude–longitude grid. While the l_∞ normalized error is slightly larger than results presented in [31], the l_1 and l_2 errors produce comparable results and there is no evidence of degradation in the simulation as the vortices pass over the corners and along face edges of the cubed-sphere. The convergence of the l_1, l_2, and l_∞ errors with increasing resolution from c48 (2°) to c768 (0.125°) is presented in Fig. 13. The convergence rates are 1.52, 1.67 and 1.54 for the l_∞, l_2, and l_1 errors respectively.
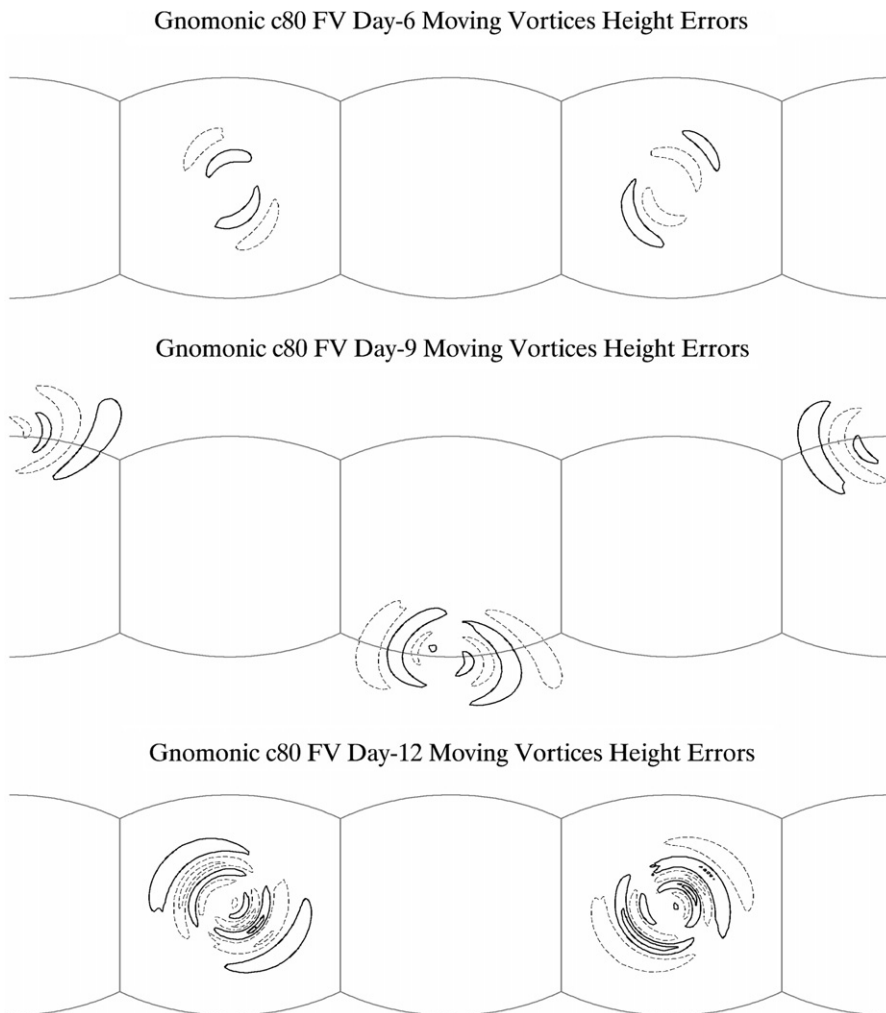

Fig. 11. Error plots from the moving vortices test case with flow oriented over the corners of the gnomonic cubed-sphere grid at c80 resolution. Errors are plotted as the difference between the simulation and the analytic solution at days 6, 9 and 12. Contours range from −0.05 to 0.05 at a 0.02 contour interval.
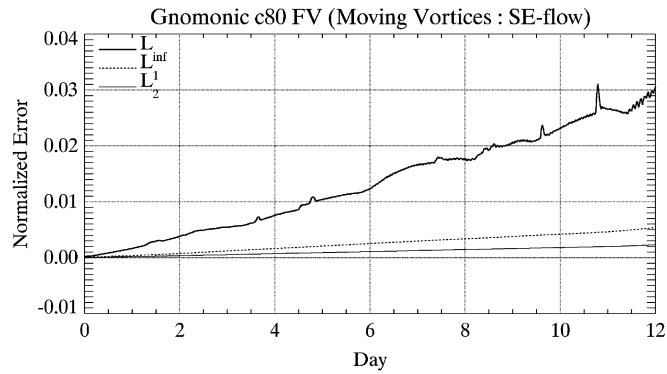
Fig. 12. Time traces of normalized l_1, l_2 and l_∞ errors for the moving vortices test case with flow oriented over the corners of the cubed-sphere for the gnomonic mapping at c80 resolution using the ORD = 7 advection scheme.
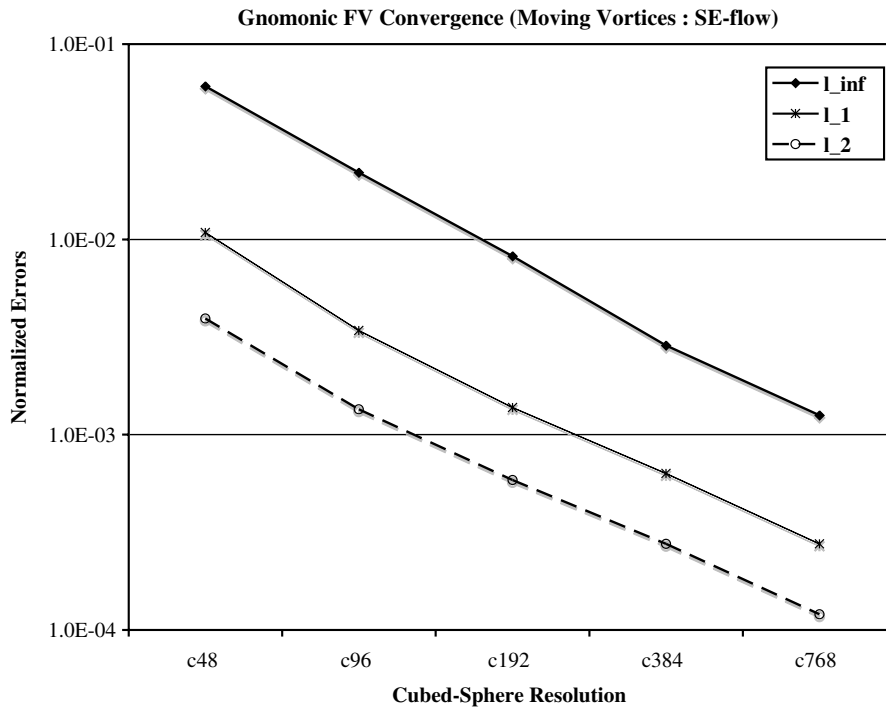

Fig. 13. Convergence of normalized l_1, l_2 and l_∞ errors for the moving vortices test case with flow oriented over the corners of the gnomonic cubed-sphere grid with the ORD = 7 advection scheme at resolutions ranging from c48 to c768.

The much sharper gradients in this test case and the increased activation of the monotonicity constraint contribute to these lower convergence rates than that of the cosine bell solid body rotation test case.

5. Summary and conclusions

The conservative multidimensional flux-form transport scheme of LR96 has been extended to the cubed-sphere geometry. Standard solid body rotation advection tests have been used to evaluate a variety of mappings for the cubed-sphere including the gnomonic, conformal, and grids modified by spring dynamics and elliptic solvers. The gnomonic cubed-sphere grid has been shown to provide a suitable framework for the discritization of the FV scheme on the cubed-sphere. A square block advection test with the monotonic

constraint demonstrated the scheme's ability to handle strong discontinuities/shocks, a feature unique to finite-volume (flux-form) schemes, and we believe it would prove to be increasingly important as resolution increases toward global cloud-resolving scales. Further evaluation via deformational flow and moving vortices test cases reveal the generalized FV scheme on the gnomonic cubed-sphere grid to be performing adequately in comparison with the original latitude–longitude implementation and a discontinuous Galerkin scheme on the cubed-sphere.

The original transport scheme of LR96 assumed an orthogonal coordinate system; as such the conformal mapping would appear to be the most ideal configuration for the finite-volume transport scheme. The convergence of minimum grid lengths on the conformal grid with increasing resolution proves to be a severe limitation on numerical stability as we approach cloud-resolving resolutions of 10 km and finer. Elliptic solvers and spring dynamics techniques have been utilized to improve the numerical efficiency of the cubed-sphere implementation by limiting the convergence of minimum grid lengths near the corner singularities. Both grid modification techniques have been tuned to effectively reduce the impact of the minimum grid length on numerical stability. The elliptic solver has been shown to scale the minimum grid length at the same rate as the ideal gnomonic grid, without compromising accuracy due to non-orthogonality and smoothness within the grid.

A non-orthogonal extension has been developed for the LR96 finite-volume transport scheme to allow the use of the highly non-orthogonal, but more uniform, gnomonic mapping. Advection results over the non-orthogonal regions near the corners of the cubed-sphere grid reveal the gnomonic grid with the non-orthogonal extension to the flux-form transport scheme to become competitive with the conformal and quasi-orthogonal elliptic and spring grids. Due to the improved uniformity of the gnomonic grid and the results presented for these advection test cases the use of the gnomonic grid is preferred for all further FV cubed-sphere development and implementation.

Alternatives to the traditional PPM schemes of [33] have been presented, including quasi-monotonic schemes using PPM with Huynh's second constraint with and without special edge treatment for the cubed-sphere, and a non-monotonic quasi-fifth-order scheme. The quasi-monotonic scheme has been shown to reduce errors in the standard advection tests for all normalized errors, while still effectively limiting over and undershoots from the numerical solution. The non-monotonic scheme leads to a dramatic decrease in the point-based infinity-norm error, while producing significant negative values on the order of (-10^{-3}). The quasi-monotonic scheme using PPM with Huynh's second constraint with special edge treatment for the cubed-sphere (ORD = 7) proves to be overall the most accurate scheme.

The convergence properties for the FV ORD = 7 scheme on the gnomonic cubed-sphere demonstrates good convergence rates, within an accepted range of the second order accuracy of the multidimensional scheme, for resolutions as coarse as 8° down to mesoscale resolutions of 0.125°. A full shallow water model on the gnomonic cubed-sphere grid has been developed and will be the subject of a future manuscript.

Acknowledgements

Appendix A. Vectors in the general curvilinear coordinate system on the cubed-sphere

In Section 2 the flux-form multidimensional transport scheme is discretized in general non-orthogonal curvilinear coordinates. The covariant and contra-variant wind vector components are presented in Eqs. (4) and (5) based on the local unit vectors $(\overrightarrow{e_1}, \overrightarrow{e_2})$ of the coordinate system. Given the angle (α) between the two unit vectors

$$\cos\alpha = \vec{e_1} \cdot \vec{e_2}, \tag{32}$$

the covariant and contravariant components are related by the following relationships:

$$u = \tilde{u} + \tilde{v}\cos\alpha, \tag{33}$$
$$v = \tilde{v} + \tilde{u}\cos\alpha, \tag{34}$$

or (solving for the contravaraint components)

$$\tilde{u} = \frac{1}{\sin^2\alpha}[u - v\cos\alpha], \tag{35}$$

$$\tilde{v} = \frac{1}{\sin^2\alpha}[v - u\cos\alpha], \tag{36}$$

The winds on the cubed-sphere can be oriented to/from local coordinate orientation to a spherical latitude–longitude component form using the local unit vectors of the curvilinear coordinate system $(\vec{e_1}, \vec{e_2})$ and the unit vector from the center of the sphere to the surface at the point of the vector location $(\vec{e_\lambda}, \vec{e_\theta})$. Eqs. (37) and (38) represent the transformation from the spherical orientation $(u_{\lambda\theta}, v_{\lambda\theta})$ to the local cubed-sphere form (u, v), and the reverse transformation is presented in Eqs. (39) and (40).

$$u = (\vec{e_1} \cdot \vec{e_\lambda})u_{\lambda\theta} + (\vec{e_1} \cdot \vec{e_\theta})v_{\lambda\theta} \tag{37}$$

$$v = (\vec{e_2} \cdot \vec{e_\lambda})u_{\lambda\theta} + (\vec{e_2} \cdot \vec{e_\theta})v_{\lambda\theta} \tag{38}$$

$$u_{\lambda\theta} = \frac{(\vec{e_2} \cdot \vec{e_\theta})u - (\vec{e_1} \cdot \vec{e_\theta})v}{(\vec{e_1} \cdot \vec{e_\lambda})(\vec{e_2} \cdot \vec{e_\theta}) - (\vec{e_2} \cdot \vec{e_\lambda})(\vec{e_1} \cdot \vec{e_\theta})} \tag{39}$$

$$v_{\lambda\theta} = \frac{(\vec{e_2} \cdot \vec{e_\lambda})u - (\vec{e_1} \cdot \vec{e_\lambda})v}{(\vec{e_1} \cdot \vec{e_\lambda})(\vec{e_2} \cdot \vec{e_\theta}) - (\vec{e_2} \cdot \vec{e_\lambda})(\vec{e_1} \cdot \vec{e_\theta})} \tag{40}$$

Appendix B. A quasi-fifth-order finite-volume scheme

The scheme is a hybrid form of [34] and the original PPM of [33], using the "fifth-order" interpolation of Suresh and Huynh (their Eq (2.1)) to obtain the edge values as needed by the PPM methodology. Given the cell mean values as q_i^n, the "right" edge (departure from cell mean) is computed as

$$q_i^+ = a_1 q_{i-2}^n + a_2 q_{i-1}^n + a_3 q_i^n + a_4 q_{i+1}^n + a_5 q_{i+2}^n \tag{41}$$

and the "left" edge (departure from cell mean) is a mirror reflection of the right edge, computed as

$$q_i^- = a_5 q_{i-2}^n + a_4 q_{i-1}^n + a_3 q_i^n + a_2 q_{i+1}^n + a_1 q_{i+2}^n \tag{42}$$

where $a_1 = 1/30$, $a_2 = -13/60$, $a_3 = -13/60$, $a_4 = 0.45$, and $a_5 = -0.05$.

The final 1D scheme (optimized for reduced floating point operations) is as follows:

$$q_i^{n+1} = q_i^n + c_{i-1/2}q_{i-1/2}^* - c_{i+1/2}q_{i+1/2}^* \tag{43}$$

for $c_{i-1/2} > 0$

$$q_{i-1/2}^* = q_{i-1}^n + (1 - c_{i-1/2})[q_{i-1}^+ - c_{i-1/2}(q_{i-1}^- + q_{i-1}^+)] \tag{44}$$

and for $c_{i-1/2} < 0$

$$q_{i-1/2}^* = q_i^n + (1 + c_{i-1/2})[q_i^- + c_{i-1/2}(q_i^- + q_i^+)] \tag{45}$$

where we defined the "upwind" CFL number as

$$c_{i-1/2} = \begin{cases} \frac{\Delta t u_{i-1/2}}{\Delta x_{i-1}}, & \text{for } u_{i-1/2} > 0 \\ \frac{\Delta t u_{i-1/2}}{\Delta x_i}, & \text{for } u_{i-1/2} < 0 \end{cases} \tag{46}$$

and u is the local wind speed.

Appendix C. Discontinuous treatment of the 12 face edges on the cubed-sphere

There are 12 interfacing edges between the 6 faces on the cubed-sphere. Regardless of the projection methods (Gnomonic, conformal, elliptic, and the spring dynamics grids), these edges where two locally continuous coordinate systems intersect are discontinuous, at least at the 8 corners of the cubed-sphere. A straightforward implementation of the PPM methodology for the construction of the subgrid distribution would potentially lead to large error. This problem is most severe with the Gnomonic projection, as it is the most discontinuous at the edges. To address this problem, we shall treat the 12 face edges as true discontinuities.

We only need to modify the subgrid reconstruction scheme for the two cells (i.e., finite-volumes) nearest to the face edges. Given the volume means on the "left" and "right" sides of the edges as q_i^l ($i = 0, -1, -2, \ldots$) and q_i^r ($i = 1, 2, 3, \ldots$), respectively, the first guess (before the application of the monotonicity constraint) at the edge (for the construction of the piecewise parabolic subgrid distribution) is computed as the average of the two one-sided second order extrapolations (extrapolations from left and right sides independently)

$$q_e = \frac{1}{2}\left[\frac{3}{2}\left(q_1^r + q_0^l\right) - \frac{1}{2}\left(q_2^r + q_{-1}^l\right)\right] \tag{47}$$

Note, the averaging process results in the form of a fourth order interpolation (as in standard PPM), only the coefficients are different.

To ensure positivity for tracers, one can, at this stage, optionally apply the following simple positive definite constraint:

$$q_e \leftarrow \max(0, q_e) \tag{48}$$

The value computed as above is shared by the two adjoining faces. Therefore, the subgrid profile is still continuous (before monotonicity constraint).

Focusing on the right face (the left face follows exactly the same procedure), the remaining task is to compute the first guess value at the other end of the cell, which is determined by fitting a cubic polynomial that meets the following four conditions: (1) vanishing second derivative at the edge discontinuity, (2) local area mean equals the given cell means at the first cell q_1^r, (3) local area mean equals the given cell means at the second (to the right of the face edge) cell q_2^r, (4) mean slope at the second cell equals that of the locally computed value from the standard PPM algorithm (for the interior), m_2^r. The resulting formula is

$$q_{e+}^r = \frac{1}{14}\left(3q_1^r + 11q_2^r - 2m_2^r\right) \tag{49}$$

The subgrid piecewise parabolic profile is completely described using q_1^r, q_e, and q_{e+}^r.

References

[1] S.-J. Lin, A "vertically Lagrangian" finite-volume dynamical core for global models, Monthly Weather Review 132 (2004) 2293–2307.

[2] S.-J. Lin, R. Atlas, K.-S. Yeh, Global weather prediction and high-end computing at NASA, Computing in Science and Engineering 6 (1) (2004) 29–35.

[3] R. Atlas, O. Oreste, B.-W. Shen, S.-J. Lin, J.-D. Chern, W. Putman, T. Lee, K.-S. Yeh, M. Bosilovich, J. Radakovich, Hurricane forecasting with the high-resolution NASA finite-volume general circulation model, Geophysical Research Letters 32 (L03807) (2006).

[4] B.-W. Shen, R. Atlas, J.-D. Chern, O. Reste, S.-J. Lin, T. Lee, J. Chang, The 0.125 degree finite-volume general circulation model on the NASA columbia supercomputer: Preliminary simulations of mesoscale vortices, Geophysical Research Letters 33 (L05801) (2006).

[5] T.L. Delworth et al., GFDL's CM2 global coupled climate models – Part I: Formulation and simulation characteristics, Journal of Climate 19 (5) (2006) 643–674.

[6] W.D. Collins, P.J. Rasch, B.A. Boville, J.J. Hack, J.R. McCaa, D.L. Williamson, B. Briegleb, C. Bitz, S.-J. Lin, M. Zhang, The formulation and atmospheric simulation of the community atmosphere model: CAM3, Journal of Climate 19 (11) (2006) 2144–2161.

[7] P.J. Rasch, D.B. Coleman, N. Mahowald, D.L. Williamson, S.-J. Lin, B.A. Boville, P. Hess, Characteristics of atmospheric transport using three numerical formulations for atmospheric dynamics in a single GCM framework, Journal of Climate 19 (11) (2006) 2243–2266.

[8] W. Putman, S.-J. Lin, B.-W. Shen, Cross-platform performance of a portable communications module the nasa finite volume general circulation model, International Journal of High Performance Computing Applications 19 (3) (2005) 213–223.

[9] R. Oehmke, Q. Stout, Parallel adaptive blocks on a sphere, in: 11th SIAM Conference on Parallel Processing for Scientific Computing, 2001.

[10] M. Herzog, C. Jablonowski, R.C. Oehmke, J.E. Penner, Q.F. Stout, B. van Leer, Adaptive grids in climate modeling: Concept and first results, Eos Trans. AGU, 84(46), Fall Meet. Suppl., Abstract A11D-01, 2003.

[11] C. Jablonowski, Adaptive grids in weather and climate modeling, Ph.D. thesis, University of Michigan (2004).

[12] R. Sadourny, Conservative finite-difference approximations of the primitive equations on quasi-uniform spherical grids, Monthly Weather Review 144 (1972) 136–144.

[13] C. Ronchi, R. Iacono, P. Paolucci, The "Cubed-Sphere:" a new method for the solution of partial differential equations in spherical geometry, Journal of Computational Physics 124 (1996) 93–114.

[14] M. Rancic, J. Purser, F. Messinger, A global shallow water model using an expanded spherical cube: Gnomonic versus conformal coordinates, Quarterly Journal of the Royal Meteorological Society 122 (1996) 959–982.

[15] J. Purser, M. Rancic, Smooth quasi-homogeneous gridding of the sphere, Quarterly Journal of the Royal Meteorological Society 124 (1998) 637–647.

[16] S.-J. Lin, R. Rood, Multidimensional flux form semi-Lagrangian transport schemes, Monthly Weather Review 124 (1996) 2046–2070.

[17] R. Sadourny, A. Arakawa, Y. Mintz, Integration of the nondivergent barotropic vorticity equation with an icosahedal-hexagonal grid for the sphere, Monthly Weather Review 96 (1968) 351–356.

[18] D. Williamson, Integration of the barotropic vorticity equation on a spherical geodesic grid, Tellus 20 (1968) 642–653.

[19] T. Ringler, R. Heikes, D. Randall, Modeling the atmospheric general circulation using a spherical geodesic grid: A new class of dynamical cores, Monthly Weather Review 128 (2000) 2471–2490.

[20] A. Khamayseh, C. Mastin, Surface grid generation based on elliptic PDE models, Applied Mathematics and Computation 65 (1994) 253–264.

[21] H. Tomita, M. Tsugawa, M. Satoh, K. Goto, Shallow water model on a modified icosahedral geodesic grid by using spring dynamics, Journal of Computational Physics 174 (2001) 579–613.

[22] P. Lauritzen, A stability analysis of finite-volume advection schemes permitting long time steps, Monthly Weather Review 135 (7) (2007) 2658–2673.

[23] W.C. Skamarock, Positive-definite and montonic limiters for unrestricted-timestep transport schemes, Monthly Weather Review 134 (2006) 2241–2250.

[24] H. Huynh, Schemes and constraints for advection, in: Fifth International Conference on Numerical Methods in Fluid Dynamics, 1996.

[25] A. Khamayseh, C. Mastin, Computational conformal mapping for surface grid generation, Journal of Computational Physics 123 (1996) 394–401.

[26] A. Adcroft, J.-M. Campin, C. Hill, J. Marshall, Implementation of an atmosphere–ocean general circulation model on the expanded spherical cube, Monthly Weather Review 132 (2004) 2845–2863.

[27] D. Williamson, J. Drake, J. Hack, R. Jakob, P. Swarztrauber, A standard test set for numerical approximations to the shallow water equations in spherical geometry, Journal of Computational Physics 102 (1992) 211–224.

[28] R. Nair, J. Cote, A. Staniforth, Cascade interpolation for semi-Lagrangian advection over the sphere, Quarterly Journal of the Royal Meteorological Society 125 (1999) 1445–1468.

[29] R. Nair, B. Machenhauer, The mass-conservative cell-integrated semi-Lagrangian advection scheme on the sphere, Monthly Weather Review 130 (2002) 649–667.

[30] R. Nair, S. Thomas, R. Loft, A discontinuous Galerkin transport scheme on the cubed sphere, Monthly Weather Review 133 (2005) 814–828.

[31] R. Nair, C. Jablonowski, Moving vortices on the sphere: A test case for horizontal advection problems, Monthly Weather Review, in press.

[32] M. Zerroukat, N. Wood, A. Staniforth, A monotonic and positive definite filter for a semi-Lagrangian Inherently Conserving and Efficient (SLICE) scheme, Quarterly Journal of the Royal Meteorological Society 131 (2005) 2923–2936.

[33] P. Collela, P. Woodward, The piecewise parabolic method (PPM) for gasdynamical simulations, Journal of Computational Physics 54 (1984) 174–201.

[34] A. Suresh, H.T. Huynh, Accurate monotonicity-preserving schemes with Runge–Kutta time stepping, Journal of Computational Physics 136 (1997) 83–99.